

Monte Carlo simulations of a disordered superconductor-metal quantum phase transition

Ahmed K. Ibrahim and Thomas Vojta

Department of Physics, Missouri University of Science and Technology, Rolla, Missouri 65409, USA

Received: / Revised version:

Abstract. We investigate the quantum phase transitions of a disordered nanowire from superconducting to metallic behavior by employing extensive Monte Carlo simulations. To this end, we map the quantum action onto a (1+1)-dimensional classical XY model with long-range interactions in imaginary time. We then analyze the finite-size scaling behavior of the order parameter susceptibility, the correlation time, the superfluid density, and the compressibility. We find strong numerical evidence for the critical behavior to be of infinite-randomness type and to belong to the random transverse-field Ising universality class, as predicted by a recent strong disorder renormalization group calculation.

PACS. 64.70.Tg 74.40.Kb

1 Introduction

Investigating the electrical transport in low-dimensional fluctuating superconductors has attracted great interest during the last decades. Early experiments [1] demonstrated nonzero resistivity below the bulk critical temperature. This was explained using the notion of thermally activated phase slips [2,3,4]. Later, quantum phase slips were considered as well [5,6]. Recent experiments [7,8,9,10,11] studied the electrical transport characteristics of one-dimensional ultrathin metallic nanowires. Measurements of the resistance demonstrated that thicker wires undergo a phase transition from a metallic state to a superconducting state upon decreasing the temperature. However, thinner wires do not show superconductivity even at the lowest temperatures T .

The behavior of these experiments can be understood using the concept of a superconductor-metal quantum phase transition (as a function of wire thickness) in the pair-breaking universality class, as proposed in recent theoretical work [12,13,14]. The pair breaking is likely caused by magnetic moments on the wire surface. The nanowires in question are narrower than the (bulk) superconducting coherence length but still contain a large number of transverse channels for unpaired electrons. The resulting theory is therefore built on a model of one-dimensional superconducting fluctuations whose dynamics is overdamped because of the coupling to three-dimensional unpaired electrons [15,16,17,18,19].

Quenched disorder plays a significant role in these nanowires due to the random positions of the pair-breaking magnetic moments. The thermodynamics of the resulting disordered superconductor-metal quantum phase transition has been studied analytically via a strong-

disorder renormalization group analysis [20,21] and numerically [14] via a solution of the saddle-point equations of the corresponding Landau-Ginzburg-Wilson (LGW) order parameter field theory. Both methods invoke the large- N limit in which the number of order parameter components is generalized from 2 (representing the real and imaginary parts of the Cooper pair density) to $N \gg 1$. These methods predict that the quantum phase transition is governed by an unconventional nonperturbative infinite-randomness critical point in the same universality class as the random transverse-field Ising model [22,23]. Its dynamical scaling is of activated rather than power-law type, i.e., the correlation time ξ_τ is related to the correlation length ξ as $\ln \xi_\tau \sim \xi^\psi$, where $\psi = 0.5$ is the tunneling exponent. Observables also show nonconventional scaling behavior. For example, the order parameter susceptibility diverges not just at criticality but in an entire parameter region, the quantum Griffiths phase, around the transition. The superfluid density on the superfluid side of the transition also behaves anomalously. It remains zero in part of the long-range ordered quantum Griffiths phase. As these results have been obtained within the large- N approximation, it is important to verify that they remain valid for the physical case of a two-component order parameter.

In this paper, we therefore investigate the effects of disorder on the quantum phase transition between superconductor and metal in thin nanowires by employing a Monte Carlo method. This allows us to test the predictions directly for $N = 2$ order parameter components. Our paper is organized as follows: In Sec. 2, we define the overdamped Cooper pair model and describe the mapping onto a classical XY Hamiltonian. In Sec. 3, we briefly summarize the renormalization group predictions. Section 4

introduces the Monte Carlo simulations. In Sec. 5, we discuss our results and compare them to the predictions of the strong-disorder renormalization group. We conclude in Sec. 6.

2 The model

The starting point of our work is a quantum LGW order parameter field theory (i.e., free energy functional) for an N -component vector order-parameter $\varphi = (\varphi_1, \dots, \varphi_N)$ in d space dimensions. (We will later set $d = 1$ and $N = 2$ as appropriate for the superconductor-metal transition in nanowires where φ represents the Cooper pair density.) The LGW action can be derived from a Hamiltonian of disordered electrons by employing standard techniques [24,25,26,27]. In the absence of quenched disorder, the action reads [20,28]

$$S = \int dy dx \varphi(x) \Gamma(x, y) \varphi(y) + \frac{u}{2N} \int dx \varphi^4(x), \quad (1)$$

where $x \equiv (\mathbf{x}, \tau)$ is a vector that includes position \mathbf{x} and imaginary time τ , $\int dx \equiv \int d^d \mathbf{x} \int d\tau$, and u is the standard quartic coefficient. The Fourier transform of the bare inverse propagator (two-point vertex) $\Gamma(x, y)$ reads

$$\Gamma(\mathbf{q}, \omega_n) = r + \xi_0^2 \mathbf{q}^2 + \gamma_0 |\omega_n|^{2/z_0}. \quad (2)$$

Here, r denotes the distance from criticality, ξ_0 is a microscopic length, ω_n represents the Matsubara frequency, and γ_0 is the damping coefficient. For the Ohmic order parameter dynamics caused by the coupling to the conduction electrons, the value of the bare dynamic exponent is $z_0 = 2$. Quenched disorder can be introduced into the action (1) by making the distance from criticality (and/or the other coefficients) a random function of real-space position, $r \rightarrow r + \delta r(\mathbf{x})$.

In preparation for the Monte Carlo simulations, we now set $d = 1$, $N = 2$ and map the quantum action onto a $(1 + 1)$ -dimensional classical XY model. This can be accomplished by discretizing space and imaginary time in the action (1) and interpreting imaginary time as another space dimension. As a result, the classical XY Hamiltonian reads:

$$H = - \sum_{i, \tau} (J_i^{(s)} S_{i, \tau} S_{i+1, \tau} + J_i^{(\tau)} S_{i, \tau} S_{i, \tau+1}) - \sum_{i, \tau, \tau'} K_{\tau, \tau'} S_{i, \tau} S_{i, \tau'}. \quad (3)$$

Here, $S_{i, \tau}$ is a classical XY spin (i.e., a two-component unit vector) at position i in space and τ in imaginary time. $J_i^{(s)}$ and $J_i^{(\tau)}$ are (random) ferromagnetic interactions between nearest neighbor spins in space and imaginary time directions, respectively. As the quenched disorder is time-independent, their values depend on the space coordinate i but not on the imaginary time coordinate τ (i.e., the disorder is columnar or perfectly correlated in

the time direction). The long-range interaction $K_{\tau, \tau'}$ in the time direction arises from the dissipative dynamics of the quantum action. It is given by

$$K_{\tau, \tau'} = \gamma |\tau - \tau'|^{-\alpha}, \quad (4)$$

where γ is the interaction amplitude while the exponent α takes the value 2 for Ohmic dissipation ($z_0 = 2$). The values of $J_i^{(s)}$, $J_i^{(\tau)}$, and $K_{\tau, \tau'}$ are determined by the parameters of the quantum action (1). However, as we are interested in the universal aspects of the phase transition only, their precise values do not matter. We therefore tune the transition by varying the temperature T of the classical XY model (3), while keeping $J_i^{(s)}$, $J_i^{(\tau)}$, and $K_{\tau, \tau'}$ constant. This classical temperature T differs from the actual (physical) temperature T_Q of the quantum system which maps onto the inverse system size in imaginary time direction, L_τ^{-1} , of the XY model (3). Under the quantum-to-classical mapping from the action (1) to the Hamiltonian (3), the superfluid density of the quantum system maps onto the spin-wave stiffness in space direction, and the compressibility maps onto the stiffness in imaginary time direction.

3 Theory

3.1 Renormalization group predictions

Hoyos et al. [20,21] performed a strong-disorder renormalization group analysis of the LGW theory (1) with quenched disorder in the large- N limit. This analysis yielded a quantum critical point of exotic infinite-randomness type that belongs to the random transverse-field Ising chain universality class [22,23]. Whereas the dynamical scaling in the absence of disorder is of power-law type, the disordered system features unconventional activated dynamical scaling characterized by an exponential relation between correlation time and length, $\ln \xi_\tau \sim \xi^\psi$ with $\psi = 0.5$.

Specifically, the strong-disorder renormalization group makes the following predictions for the finite-size scaling behavior of observables (see also Refs. [29,30]). Right at criticality, the order parameter susceptibility χ is expected to depend on the system size L_τ in imaginary time direction via

$$\chi \sim L_\tau [\ln(L_\tau/b)]^{2\phi-1/\psi}, \quad (5)$$

where $\phi = (1 + \sqrt{5})/2$ and $\psi = 1/2$ are the cluster size and tunneling critical exponents of the infinite-randomness critical point, respectively (b is an arbitrary microscopic scale). The logarithmic L_τ dependence in (5) reflects the activated dynamical scaling. In the ordered Griffiths phase ($T < T_c$), the susceptibility diverges as

$$\chi \sim L_\tau^{1+1/z}, \quad (6)$$

and in the disordered Griffiths phase ($T > T_c$), it behaves as

$$\chi \sim L_\tau^{1-1/z}. \quad (7)$$

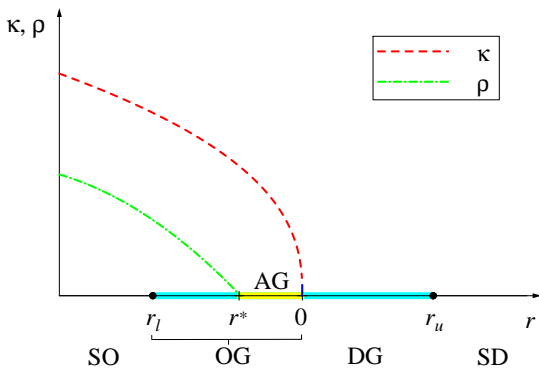


Fig. 1. Schematic behavior of the compressibility κ and the superfluid density ρ near the quantum phase transition. r denotes the distance from criticality. In the classical XY model (3), κ and ρ are represented by the spin-wave stiffnesses $\rho_s^{(\tau)}$ and $\rho_s^{(s)}$, respectively, and $r \sim T - T_c$. The strongly ordered and disordered conventional phases are marked by SO and SD whereas OG and DG are the ordered and disordered Griffiths phases. The superfluid density vanishes in the anomalous part (AG) of the ordered Griffiths phase.

The nonuniversal Griffiths dynamical exponent z varies with temperature. Upon approaching the critical point, it diverges as

$$z \sim |T - T_c|^{-\nu\psi}. \quad (8)$$

where $\nu = 2$ is the correlation length exponent of the infinite-randomness critical point.

The spin-wave stiffness ρ_s of the XY Hamiltonian describes the change in the free-energy density f during a twist of the spins at two opposite boundaries by an angle θ . For small θ and large system size l , the free-energy change reads

$$f(\theta) - f(0) = \frac{\rho_s \theta^2}{2 l^2}. \quad (9)$$

We need to distinguish two kinds of stiffnesses, the space-stiffness $\rho_s^{(s)}$, and the time-stiffness $\rho_s^{(\tau)}$. To discuss the space-stiffness $\rho_s^{(s)}$ (which corresponds to the superfluid density of the original quantum system), we implement the twist between 0 and L in space direction with $l = L$ in Eq. (9). For the time-stiffness $\rho_s^{(\tau)}$ (which corresponds to the compressibility of the quantum system), the twisted boundary conditions are between 0 and L_τ in imaginary-time direction, and $l = L_\tau$.

Both stiffnesses vanish in the disordered phase above T_c . In a conventional phase transition scenario, they would be expected to be nonzero everywhere in the long-range ordered phase below T_c . However, the theory developed in Refs. [29,31] implies anomalous behavior of $\rho_s^{(s)}$: Because the distribution of the effective interactions $J_{eff}^{(s)}$ becomes very broad under the renormalization group, the stiffness vanishes for $L \rightarrow \infty$ in part of the ordered Griffiths phase between T_c and T^* where T^* is the temperature where the Griffiths dynamical exponent $z = 1$ (see schematic Fig. 1). In this temperature range, it behaves as

$$\rho_s^{(s)} \sim L^{1-z}. \quad (10)$$

Normal behavior with nonzero $\rho_s^{(s)}$ in the thermodynamic limit is restored for $T < T^*$. In contrast, the time-stiffness $\rho_s^{(\tau)}$ is nonzero everywhere in the ordered phase, and behaves as

$$\rho_s^{(\tau)} \sim |T - T_c|^\beta, \quad (11)$$

where $\beta = 2 - \phi$ is the exponent of the order parameter.

4 Monte Carlo simulations

To confirm the predictions of the strong-disorder renormalization group summarized in Sec. 3, we perform extensive Monte Carlo simulations of the (1+1)-dimensional XY Hamiltonian (3) with long-range interactions in time direction.

We employ the Luijten algorithm [32], a version of the Wolff cluster algorithm [33] that is optimized for long-range interactions. Its numerical effort (per sweep) scales linearly with the total number of sites $N_s = L L_\tau$ (rather than $L L_\tau^2$ as expected in a naive implementation of the Wolff algorithm for long-range interactions). Using this method, we simulate systems with linear size $L = 20$ to 160 in the space direction and $L_\tau = 2$ to 40000 in the (imaginary) time direction. To introduce quenched disorder that is perfectly correlated in the imaginary time direction, we treat the interactions $J_i^{(s)}$ and $J_i^{(\tau)}$ as independent random variables derived from a binary probability distribution

$$\rho(J) = (1 - c)\delta(J - J_l) + c\delta(J - J_h) \quad (12)$$

having a higher value J_h and a lower value J_l . The concentrations of J_h and J_l are c and $(1 - c)$, respectively. In most of the simulations, we choose parameters $c = 0.5$, $J_h = 2$ and $J_l = 0.5$, and an interaction amplitude $\gamma = 0.1$ of the long-range temporal interaction.

For each simulation run we perform 100 Monte Carlo sweeps for equilibration (one sweep is defined as a number of cluster flips such that the total number of flipped spins equals the total number $N_s = L L_\tau$ of sites). We have confirmed that this is sufficient by comparing the results of runs with hot starts (spins initially pointing in random directions) and cold starts (spins initially aligned). We then perform 200 sweeps during which we measure the energy, specific heat, order parameter, susceptibility, Binder cumulant, correlation function, correlation length as well as the space and time stiffnesses (with a measurement taken after every sweep). All observables are averaged over 1000 to 10 000 disorder configurations. Using short measurement runs for a large number of disorder configurations improves the overall performance, as is discussed in Refs. [34,35,36,37].

5 Results

5.1 Clean system

To test our simulation method and to make contact with the literature, we first analyze the clean case with uniform $J_i^{(s)} = J_i^{(\tau)} = 1$. We compute the order parameter

$$m = \frac{1}{N_s} \sum_{i,\tau} S_{i,\tau}. \quad (13)$$

and its Binder cumulant [38,39]

$$g = 1 - \frac{\langle m^4 \rangle}{3\langle m^2 \rangle^2}. \quad (14)$$

We use the finite-size scaling method [40,41] to estimate the location of the critical point. The Binder cumulant is expected to have a finite-size scaling form of

$$g(r, L, L_\tau) = \Upsilon_g(rL^{1/\nu_{cl}}, L_\tau/L^{z_{cl}}). \quad (15)$$

Here, $r = T - T_c$ is the distance from the critical point, Υ_g is the scaling function, ν_{cl} is the clean correlation length exponent, and z_{cl} is the clean dynamical exponent.

The long-range interactions break the symmetry between the space and imaginary time directions, implying that the spatial and temporal system sizes L and L_τ scale differently. The value of z_{cl} is therefore not known at the outset, and we need to perform anisotropic finite-size scaling. We employ the iterative method outlined in Refs. [42, 43, 44, 45]: The Binder cumulant has a maximum as a function of L_τ for fixed L . According to (15), the peak position L_τ^{max} must behave as $L^{z_{cl}}$ at criticality, and the value g^{max} of the maximum must be L -independent. The sizes L and L_τ^{max} in the space and imaginary-time directions define the ‘‘optimal shape’’ for finite-size scaling.

Fig. 2 shows the behavior of the Binder cumulant g as a function of L_τ for several system sizes L at the estimated critical temperature $T_c = 0.56969(6)$. These curves indeed have identical maximum values that are independent of the system size L (because of corrections to scaling, some deviations occur at small L). To test the scaling form of the Binder cumulant (15) and to measure the clean dynamical exponent z_{cl} , we plot the data of the Binder cumulant as a function of $L_\tau/L^{z_{cl}}$ and vary z_{cl} until a good collapse is achieved. As shown in Fig. 3, the data collapse onto each other for a dynamical exponent value $z_{cl} = 2.01(6)$. This also implies that the dynamical scaling is of conventional power-law form, as expected [46, 47].

To compute further critical exponents of the system, we analyze the properties of the order parameter, its susceptibility, and the slope dg/dT of the Binder cumulant at the critical temperature. The correlation length exponent ν can be estimated from the slopes of Binder cumulant. Taking the derivative with respect to temperature in (15), it follows that dg/dT at criticality ($r = 0$) behaves as $L^{1/\nu_{cl}}$ (if evaluated for the optimal sample shapes $L_\tau = L_\tau^{max} \sim L^{z_{cl}}$). In Fig. 4, we plot the

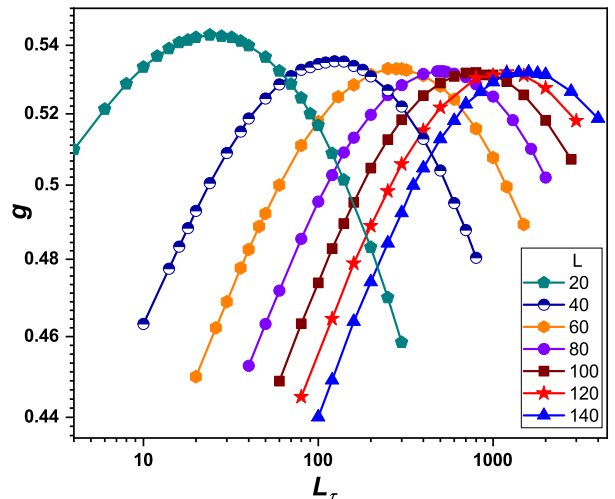


Fig. 2. Binder cumulant g of the clean system vs. L_τ for different L at the critical temperature $T_c = 0.56969$. The interactions are uniform, $J_i^{(s)} = J_i^{(\tau)} = 1$ and $\gamma = 0.1$. The statistical error of g is much smaller than the symbol size.

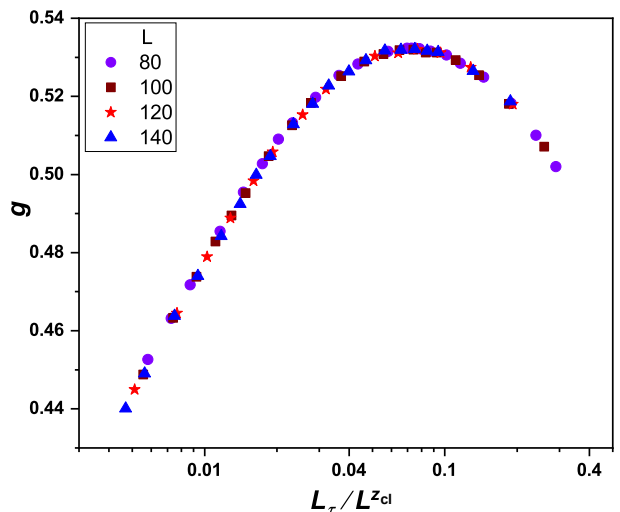


Fig. 3. Scaling plot of the Binder cumulant data from Fig. 2. It shows g as a function of $L_\tau/L^{z_{cl}}$ for different L at $T_c = 0.56969$. All curves collapse and follow the power-law scaling form (15) for $z_{cl} = 2.01$.

slopes as a function of system size L . The critical exponent $\nu_{cl} = 0.687(9)$ follows from a power-law fit of these data to $dg/dT \sim L^{1/\nu_{cl}}$. We also study the system-size dependence of the order parameter and its susceptibility at the critical temperature, as shown in Fig. 4. We find that these observables feature the expected power-law behavior (if evaluated for the optimal sample shapes $L_\tau = L_\tau^{max} \sim L^{z_{cl}}$), $m \sim L^{-\beta_{cl}/\nu_{cl}}$ and $\chi \sim L^{\gamma_{cl}/\nu_{cl}}$ [40]. Using power-law fits, we estimate the critical exponents to be $\beta_{cl}/\nu_{cl} = 0.507(5)$ and $\gamma_{cl}/\nu_{cl} = 2.03(4)$.

The exponents β_{cl}/ν_{cl} , γ_{cl}/ν_{cl} , and z_{cl} are not independent of each other. They are connected by the hyper-

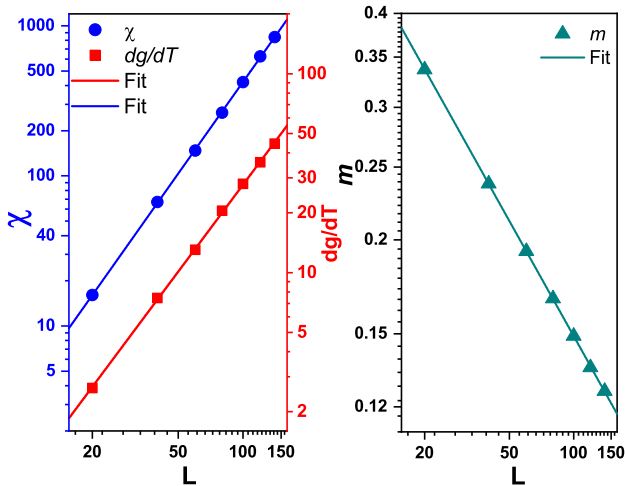


Fig. 4. Left: Double logarithmic plot of susceptibility χ and slope of Binder cumulant dg/dT vs. system size L for optimally shaped clean samples at criticality. The solid lines are fits to the predicted power laws $\chi \sim L^{\gamma/\nu}$ and $dg/dT \sim L^{1/\nu_{cl}}$ with $\gamma_{cl}/\nu_{cl} = 2.03$ and $1/\nu_{cl} = 1.454$. Right: Magnetization m as a function of L at criticality. The slope of the fitted line with $m \sim L^{-\beta_{cl}/\nu}$ gives $\beta_{cl}/\nu_{cl} = 0.507$.

scaling relation [48]

$$\frac{2\beta_{cl}}{\nu_{cl}} + \frac{\gamma_{cl}}{\nu_{cl}} = d + z_{cl} \quad (16)$$

where $d = 1$ is the number of space dimensions. We find that our numerical estimates fulfill the hyper-scaling relation within their error bars. Moreover, all clean exponents agree with those found in Ref. [47].

Note that the correlation length exponent $\nu_{cl} = 0.687$ violates the Harris criterion $d\nu_{cl} > 2$ [49], implying that the clean critical behavior will be unstable against disorder.

5.2 Disordered system

After studying and analyzing the behavior of the clean critical point, we now apply quenched disorder to the Hamiltonian (3) by making the ferromagnetic interactions $J_i^{(s)}$ and $J_i^{(\tau)}$ random functions of the space coordinate i , drawn from the probability distribution (12). We have attempted to use the same Binder-cumulant-based finite-size scaling method as in the clean case to find the critical point. Unfortunately, this analysis is hampered by strong corrections to scaling. We have therefore turned to analyzing the dependence of the order parameter susceptibility on L_τ (see Eqs. 5, 6 and 7), in analogy to Ref. [30] where similar difficulties were encountered. To test Eqs. (6) and (7), one needs to take samples having effectively infinite size L in the space direction ($L \gg L_\tau$). We have performed simulations with system size $L = 1000$ and $L_\tau = 10$ to 224. Fig. 5 confirms that χ behaves as a power of L_τ for an entire range of temperatures (the Griffiths region), as predicted theoretically in eqs. (6) and (7). The Griffiths

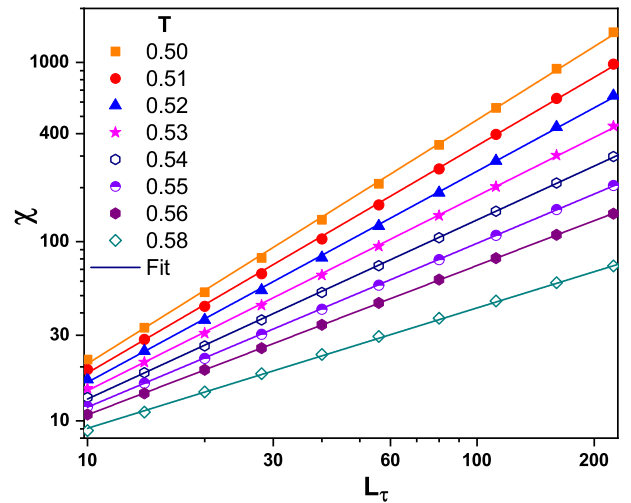


Fig. 5. Susceptibility χ of the disordered system as a function of L_τ for various temperatures in the Griffiths phase. The size in space direction is $L = 1000$. The solid lines are fits to the power laws (6) and (7).

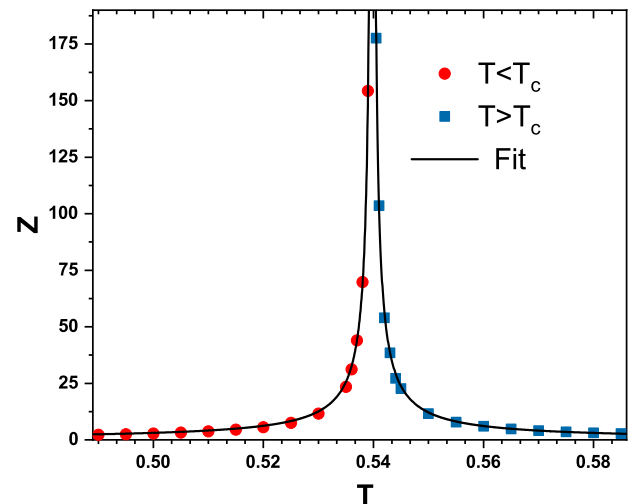


Fig. 6. Dynamical exponent z as a function of classical temperature T in Griffiths regions. The data are extracted from the susceptibility data in Fig. 5. The solid lines are fits of z to Eq. (17).

dynamical exponent z can be determined by fitting the susceptibility to eqs. (6) and (7). Its value is predicted to vary with temperature and to diverge at the critical point as

$$z \sim \frac{1}{|T - T_c|}. \quad (17)$$

Fig. 6 shows the values of z in the ordered and disordered Griffiths phase as a function of temperature T . These values are fitted to the power law relation (17) giving an estimated critical temperature of $T_c \approx 0.540(9)$.

In addition to the order parameter susceptibility, we also investigate the superfluid density and the compressibility of the quantum system. In the classical problem (3), they are represented by the spin-wave stiffnesses in

the space and time directions, respectively. The spatial stiffness can be computed using the relation [50]

$$\rho_s^{(s)} = \frac{1}{N_s} \sum_{i,j,\tau,\tau'} J_{i,j,\tau,\tau'} \langle \mathbf{S}_{i,\tau} \cdot \mathbf{S}_{j,\tau'} \rangle (i-j)^2 - \frac{1}{N_s T} \left\langle \left(\sum_{i,j,\tau,\tau'} J_{i,j,\tau,\tau'} \hat{\mathbf{K}} \cdot (\mathbf{S}_{i,\tau} \times \mathbf{S}_{j,\tau'}) (i-j) \right)^2 \right\rangle, \quad (18)$$

where

$$J_{i,j,\tau,\tau'} = \begin{cases} J_i^{(s)} & \text{if } j = i \pm 1, \tau = \tau' \\ J_i^{(\tau)} & \text{if } i = j, \tau = \tau' \pm 1 \\ \gamma |\tau - \tau'|^{-\alpha} & \text{if } i = j, \tau \neq \tau' \\ 0 & \text{otherwise} \end{cases},$$

Here, $N_s = LL_\tau$ is the total number of sites, and $\hat{\mathbf{K}}$ is the unit vector perpendicular to the xy -plane in spin space. For the calculation of $\rho_s^{(\tau)}$, the term $(i-j)$ has to be replaced by $(\tau - \tau')$.

The behavior of the spin-wave stiffnesses is illustrated in Fig. 7. It shows the results for the space and time stiffness of a system of size $L = 160$ and $L_\tau = 10000$. Clearly, the two stiffnesses behave differently. According to Eq. (11), the imaginary-time stiffness (i.e., the compressibility of the original quantum system) is expected to behave as $|T - T_c|^\beta$, i.e., it vanishes at T_c . Despite significant finite-size rounding, our data are qualitative compatible with this prediction, giving $T_c \approx 0.53$, in agreement with our earlier estimate of $T_c = 0.540(9)$. In contrast, the space stiffness $\rho_s^{(s)}$ is more than two orders of magnitude smaller even though the microscopic interaction strengths do not have a significant anisotropy. Moreover, $\rho_s^{(s)}$ vanishes at a lower temperature $T^* \approx 0.50$, giving rise to anomalous elasticity [31] for temperatures between T_c and T^* .

In addition, we compute the correlation function G in the space and time directions to determine the corresponding correlation lengths ξ and ξ_τ , respectively. This allows us to estimate the correlation length exponent ν . The correlation functions in space and time directions are defined as

$$G(x) = \frac{1}{N_s} \sum_{i,j,\tau} \langle \mathbf{S}_{i,\tau} \cdot \mathbf{S}_{j,\tau} \rangle \delta(x - |i - j|), \quad (19)$$

$$G(\tau) = \frac{1}{N_s} \sum_{i,\tau_1,\tau_2} \langle \mathbf{S}_{i,\tau_1} \cdot \mathbf{S}_{i,\tau_2} \rangle \delta(\tau - |\tau_1 - \tau_2|). \quad (20)$$

Fig. 8 shows the spatial correlation function (19) for different temperatures in the Griffiths region above T_c for a system of sizes $L = 80$ and $L_\tau = 1200$. Because of the small spatial system size, there are significant finite-size effects for temperatures close to $T_c = 0.54$ for which the correlations decay slowly (notice the unexpected up-turns for large $|\mathbf{x}|$ of the correlation functions for the lower temperatures). The strong-disorder renormalization group

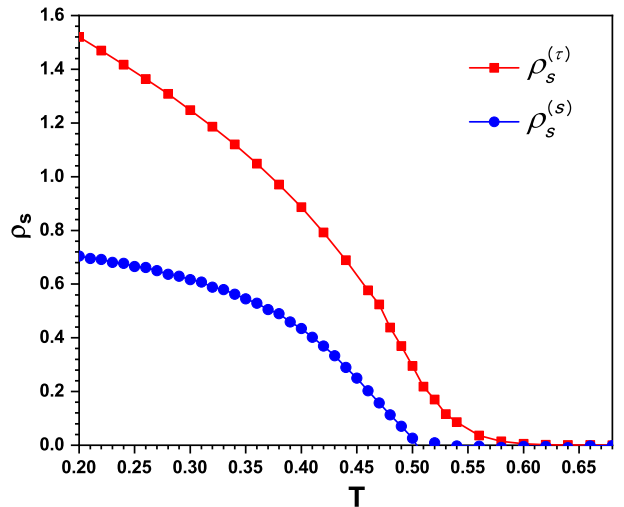


Fig. 7. Spin-wave stiffness in space $\rho_s^{(s)}$ and time $\rho_s^{(\tau)}$ as function of the classical temperature T with system size $L = 160$ and $L_\tau = 10000$. The data for $\rho_s^{(s)}$ are rescaled by 500 for clarity.

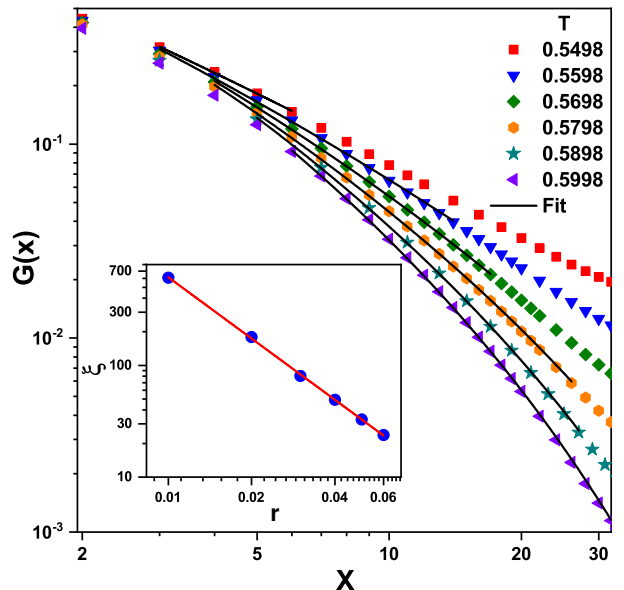


Fig. 8. Space-correlation function $G(x)$ for several temperatures in Griffiths phase. The solid lines are fits to Eq. (21). Inset: The space-correlation length ξ obtained by analyzing space-correlation function as a function of distance δ from critical temperature. The solid line is a fit of Eq. (22).

[23] predicts that the spatial correlation function behaves as

$$G(x) \sim \frac{\exp[-(x/\xi) - (27\pi^2/4)^{1/3}(x/\xi)^{1/3}]}{(x/\xi)^{5/6}}. \quad (21)$$

The figure shows that $G(x)$ is well described by this functional form for temperatures away from T_c . Closer to T_c , the agreement becomes questionable, because the finite-size effects restrict the fits to a very narrow $|\mathbf{x}|$ -range. Ignoring these complications, we can extract values of ξ

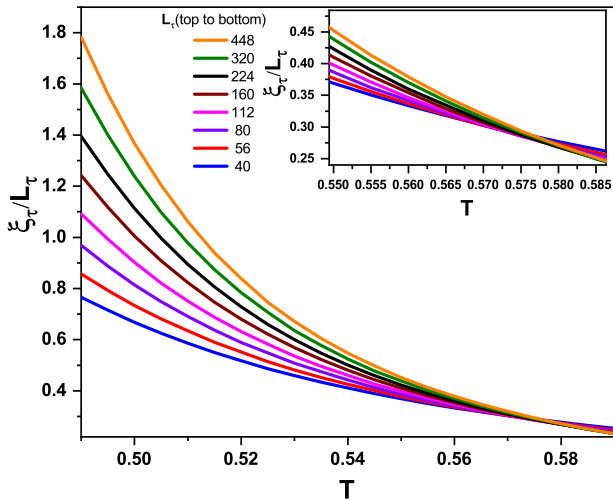


Fig. 9. Scaled correlation time ξ_τ/L_τ versus temperature T for different values of L_τ in the Griffiths region. The system size in space is $L = 1000$; the data are averaged over 2000 disorder configurations. The inset shows a magnification for the crossing point of the curves.

by fitting the $G(x)$ data to Eq. (21) for distances between $x = 3$ and some cutoff at which the curves start to become noisy or deviate from the expected behavior. The inset of Fig. 8 shows the relation between the correlation length ξ and the distance from criticality $r = T - T_c$ which reads [23]

$$\xi \sim |r|^{-\nu}. \quad (22)$$

As expected, the data can be fitted to the power law (22), giving a correlation length exponent of $\nu = 1.8(3)$, in reasonable agreement with the renormalization group result $\nu = 2$ [23].

We also analyze the average correlation time ξ_τ . As we can reach much larger temporal system sizes L_τ than spatial system sizes L , we can compute ξ_τ via the standard second-moment method [51, 52, 53] from the Fourier transform $\tilde{G}(\omega)$ of the temporal correlation function $G(\tau)$:

$$\xi_\tau = \left[\frac{\tilde{G}(0) - \tilde{G}(\omega_{min})}{\omega_{min}^2 \tilde{G}(\omega_{min})} \right]^{1/2}. \quad (23)$$

Here, ω_{min} is the minimum wave number, $2\pi/L_\tau$ in the imaginary-time direction.

The behavior of the correlation time ξ_τ in the Griffiths phase is illustrated by plotting ξ_τ/L_τ as a function of temperature T for several system of size L_τ , as shown in Fig. 9. Remarkably, the different curves cross at temperature $T \approx 0.578$, clearly much higher than our critical temperature $T_c \approx 0.54$. This indicates that the correlation time ξ_τ diverges in part of the disordered phase before reaching the phase transition. This behavior is indicative of infinite-randomness physics and can be understood by estimating the rare region contribution to the correlation

time ξ_τ [30]. It reads

$$\xi_\tau \sim \int_0^{\epsilon_0} d\epsilon \epsilon^{1/z-1} \frac{1}{\epsilon}, \quad (24)$$

where ϵ is the renormalized distance from criticality of rare region and the factor $\epsilon^{1/z-1}$ stems from the rare-region density of states. According to Eq. (24), the integral diverges for $z > 1$ and converges for $z < 1$. Therefore, the correlation time is expected to diverge in the disordered Griffiths phase (before reaching the phase transition) at the temperature at which the Griffiths dynamical exponent is $z = 1$.¹

6 Conclusions

In summary, we have studied the superconductor to metal quantum phase transition in ultra thin nanowires by performing large-scale Monte Carlo simulations. To this end, we have mapped the quantum action onto a (1+1)-dimensional classical XY Hamiltonian with long-rang interactions and columnar disorder.

For the clean system, we have employed finite-size scaling of the Binder cumulant to estimate the critical point and determine the universality class of the phase transition. Our results agree well with earlier Monte-Carlo simulations [47] as well as perturbative renormalization group results [46, 12]. In particular, the dynamical scaling is of conventional power-law type $\xi_\tau \sim \xi^{z_{cl}}$.

In the presence of quenched disorder, our results provide strong evidence in support of the exotic infinite-randomness behavior that was predicted by the strong-disorder renormalization group approach [20] and the large- N saddle point analysis [14]. It features activated dynamical scaling, $\ln \xi_\tau \sim \xi^\psi$. In particular, the critical behavior is compatible with the universality class of the random transverse-field Ising chain. This may appear surprising at first glance because the random transverse-field Ising model has discrete symmetry and no dissipation while our current problem has continuous XY symmetry and Ohmic dissipation. However, the behavior agrees with the general classification of disordered quantum phase transitions developed in Refs. [54, 55, 56, 57]. In both systems, the rare regions are right at the lower critical dimension of the problem, putting the transitions into class B [57]. Moreover, both clean transitions violate the Harris criterion, implying that the disordered transitions are in subclass $B2$ which features infinite-randomness criticality [57].

Rare regions also lead to unusual properties in the Griffiths phases on both sides of the phase transition. Specifically, the superfluid density vanishes in part of the long-range ordered (superfluid) Griffiths phase, giving rise to

¹ The agreement between the crossing temperature in Fig. 9, and the temperature at which the susceptibility-based z -value (see Fig. 6) equals 1 is not particularly good. This can be attributed to strong corrections to scaling, manifest, e.g., in the drift with L_τ of the crossing in Fig. 9.

an anomalous (sliding) Griffiths phase with unusual elastic properties [31, 58]. On the disordered side of the transition, rare regions lead to a divergence of the average correlation time before the transition is reached.

Our Monte Carlo simulations can in principle be generalized to compute further observables including the dynamical conductivity in the regime $\omega \gg T$. This would allow us to test the predictions of Ref. [28]. Due to the large numerical effort, this remains a task for the future.

This work was supported by the NSF under Grants No. DMR-1506152, PHY-1125915 and PHY-1607611. Thomas Vojta is thankful for the hospitality of the Kavli Institute for Theoretical Physics, Santa Barbara, and the Aspen Center for Physics where parts of the work were performed.

Author contribution statement

T.V. conceived and coordinated the study. A.K.I. performed the Monte Carlo simulations, analyzed the data, and created the figures. A.K.I. and T.V. wrote the manuscript.

References

1. W.W. Webb, R.J. Warburton, Phys. Rev. Lett. **20**, 461 (1968)
2. W.A. Little, Phys. Rev. **156**, 396 (1967)
3. J.S. Langer, V. Ambegaokar, Phys. Rev. **164**, 498 (1967)
4. D.E. McCumber, B.I. Halperin, Phys. Rev. B **1**, 1054 (1970)
5. N. Giordano, Phys. Rev. Lett. **61**, 2137 (1988)
6. A.D. Zaikin, D.S. Golubev, A. van Otterlo, G.T. Zimányi, Phys. Rev. Lett. **78**, 1552 (1997)
7. C.N. Lau, N. Markovic, M. Bockrath, A. Bezryadin, M. Tinkham, Phys. Rev. Lett. **87**(21), 217003 (2001)
8. G.R. Boogaard, A.H. Verbruggen, W. Belzig, T.M. Klapwijk, Phys. Rev. B **69**, 220503 (2004)
9. A. Rogachev, A.T. Bollinger, A. Bezryadin, Phys. Rev. Lett. **94**, 017004 (2005)
10. F. Altomare, A.M. Chang, M.R. Melloch, Y. Hong, C.W. Tu, Phys. Rev. Lett. **97**, 017001 (2006)
11. A. Rogachev, T.C. Wei, D. Pekker, A.T. Bollinger, P.M. Goldbart, A. Bezryadin, Phys. Rev. Lett. **97**, 137001 (2006)
12. S. Sachdev, P. Werner, M. Troyer, Phys. Rev. Lett. **92**, 237003 (2004)
13. A. Del Maestro, B. Rosenow, N. Shah, S. Sachdev, Phys. Rev. B **77**, 180501 (2008)
14. A. Del Maestro, B. Rosenow, M. Müller, S. Sachdev, Phys. Rev. Lett. **101**, 035701 (2008)
15. I.F. Herbut, Phys. Rev. Lett. **85**, 1532 (2000)
16. A.V. Lopatin, N. Shah, V.M. Vinokur, Phys. Rev. Lett. **94**, 037003 (2005)
17. B. Spivak, A. Zyuzin, M. Hruska, Phys. Rev. B **64**, 132502 (2001)
18. M.V. Feigel'man, A.I. Larkin, M.A. Skvortsov, Phys. Rev. Lett. **86**, 1869 (2001)
19. V. Galitski, Phys. Rev. Lett. **100**, 127001 (2008)
20. J.A. Hoyos, C. Kotabage, T. Vojta, Phys. Rev. Lett. **99**, 230601 (2007)
21. T. Vojta, C. Kotabage, J.A. Hoyos, Phys. Rev. B **79**, 024401 (2009)
22. D.S. Fisher, Phys. Rev. Lett. **69**, 534 (1992)
23. D.S. Fisher, Phys. Rev. B **51**, 6411 (1995)
24. J. Hertz, Phys. Rev. B **14**, 1165 (1976)
25. A.J. Millis, Phys. Rev. B **48**, 7183 (1993)
26. T.R. Kirkpatrick, D. Belitz, Phys. Rev. Lett. **76**, 2571 (1996)
27. D. Belitz, T.R. Kirkpatrick, T. Vojta, Rev. Mod. Phys. **77**, 579 (2005)
28. A. Del Maestro, B. Rosenow, J.A. Hoyos, T. Vojta, Phys. Rev. Lett. **105**, 145702 (2010)
29. P. Mohan, R. Narayanan, T. Vojta, Phys. Rev. B **81**, 144407 (2010)
30. F. Hrahsheh, H. Barghathi, T. Vojta, Phys. Rev. B **84**, 184202 (2011)
31. P. Mohan, P.M. Goldbart, R. Narayanan, J. Toner, T. Vojta, Phys. Rev. Lett. **105**, 085301 (2010)
32. E. Luijten, H.W.J. Blöte, Int. J. Mod. Phys. C **6**, 359 (1995)
33. U. Wolff, Phys. Rev. Lett. **62**, 361 (1989)
34. H.G. Ballesteros, L.A. Fernández, V. Martín-Mayor, A. Muñoz Sudupe, G. Parisi, J.J. Ruiz-Lorenzo, Phys. Rev. B **58**, 2740 (1998)
35. H.G. Ballesteros, L.A. Fernandez, V. Martin-Mayor, A. Munoz Sudupe, G. Parisi, J.J. Ruiz-Lorenzo, Nucl. Phys. B **512**, 681 (1998)
36. T. Vojta, R. Sknepnek, Phys. Rev. B **74**, 094415 (2006)
37. Q. Zhu, X. Wan, R. Narayanan, J.A. Hoyos, T. Vojta, Phys. Rev. B **91**, 224201 (2015)
38. K. Binder, Z. Phys. B **43**(2), 119 (1981)
39. K. Binder, D.P. Landau, Phys. Rev. B **30**, 1477 (1984)
40. M.N. Barber, in *Phase Transitions and Critical Phenomena*, vol. 8, ed. by C. Domb, J.L. Lebowitz (Academic, New York, 1983), pp. 145–266
41. J. Cardy (ed.), *Finite-size scaling* (North Holland, Amsterdam, 1988)
42. M. Guo, R.N. Bhatt, D.A. Huse, Phys. Rev. Lett. **72**, 4137 (1994)
43. H. Rieger, A.P. Young, Phys. Rev. Lett. **72**, 4141 (1994)
44. R. Sknepnek, T. Vojta, M. Vojta, Phys. Rev. Lett. **93**, 097201 (2004)
45. T. Vojta, J. Crewse, M. Puschmann, D. Arovos, Y. Kiselev, Phys. Rev. B **94**, 134501 (2016)
46. S. Pankov, S. Florens, A. Georges, G. Kotliar, S. Sachdev, Phys. Rev. B **69**, 054426 (2004)
47. P. Werner, M. Troyer, S. Sachdev, J. Phys. Soc. Jpn. **74**(Suppl), 67 (2005)
48. M.A. Continentino, G.M. Japiassu, A. Troper, Phys. Rev. B **39**, 9734 (1989)
49. A.B. Harris, J. Phys. C **7**, 1671 (1974)
50. S. Teitel, C. Jayaprakash, Phys. Rev. B **27**, 598 (1983)
51. F. Cooper, B. Freedman, D. Preston, Nucl. Phys. B **210**, 210 (1982)
52. J.K. Kim, Phys. Rev. Lett. **70**, 1735 (1993)
53. S. Caracciolo, A. Gambassi, M. Gubinelli, A. Pelissetto, Eur. Phys. J. B **20**, 255 (2001)
54. T. Vojta, J. Schmalian, Phys. Rev. B **72**, 045438 (2005)
55. T. Vojta, J. Phys. A **39**, R143 (2006)
56. T. Vojta, AIP Conference Proceedings **1550**(1), 188 (2013)
57. T. Vojta, J.A. Hoyos, Phys. Rev. Lett. **112**, 075702 (2014)
58. D. Pekker, G. Refael, E. Demler, Phys. Rev. Lett. **105**, 085302 (2010)